 doi:10.20944/preprints202207.0247.v1

Article

Fault Detection and Isolation of Landing Gear Retraction/ Extension Hydraulic System Based on BG and GARRs

Yuyuan Cao*,†, Shixuan Duan†, Yanjun Li, Xudong Li, Zejian Zhao and Xingye Wang

College of Civil Aviation, Nanjing University of Aeronautics and Astronautics, Nanjing 210016, China; caoyuyuan@nuaa.edu.cn (Y.C.); a1060586733@nuaa.edu.cn (S.D.); lyj@nuaa.edu.cn (Y.L.); lixudong@nuaa.edu.cn (X.L.); nuaazzj2020@nuaa.edu.cn (Z.Z.); nuaawxy@163.com (X.W.)

* Correspondence: caoyuyuan@nuaa.edu.cn

† Co-first author.

Featured Application: With the help of the global analytic redundancy relations (GARRs), a fault signature matrix (FSM) is generated for landing gear retraction/extension (R/E) hydraulic system and the effect of progressive failures on hydraulic resistance is identified.

Abstract: Considering the landing gear's R/E hydraulic system is nonlinear in nature, identifying and isolating its defects is not straightforward. Using the power bond graph (BG), analytical redundancy relations (ARRs) are derived based on the fundamental principle of energy conservation. Boolean logic variables are then introduced to describe the operating state of the system, and finally, global analytic redundancy relations (GARRs) are produced. It is given the corresponding residuals from the GARRs and mapped to the fault signature matrix (FSM) for the purpose of assessing its detectability and isolation. Different progressive types of deficiencies have been studied, including filter blockage, actuator leaks, and landing gear selector valve reversing stuck. The residuals against threshold range results for the injected faults calculated in MATLAB/Simulink showed that this method can considerably detect the faults. In complex nonlinear systems, such as landing gear R/E hydraulic systems, the research methodology can be used to detect faults and monitoring of statuses.

Keywords: fault detection and isolation; landing gear retraction/extension hydraulic system; global analytic redundancy relations; fault signature matrix; residuals; thresholds

1. Introduction

Modern civil airplanes only have one set takeoff and landing device, the landing gear, and typically do not have redundant designs; instead, they only have backup systems, including manual extension [1–5]. Because of this, the aircraft landing gear's retraction/extension (R/E) hydraulic system is a crucial component whose operation has a direct bearing on the security of takeoff and landing. More than 50% of fatal accidents occur during the final approach and landing phases, according to statistical reports released by Boeing, Airbus, EASA (European Union Aviation Safety Agency), and ICAO (International Civil Aviation Organization) [6-9]. For this reason, it is essential to research the fault detection and isolation of the landing gear retraction/extension (R/E) hydraulic system.

Landing gear R/E hydraulic system is one of the hydraulic systems, for which fault diagnosis research methods are generally classified as knowledge-based, data-driven or model-based [10]. Most often, model-based fault diagnosis techniques are used to diagnose faults in dynamic systems. Using various modeling techniques, the object under study is modeled, including simulation models, bond graph (BG) models, and mathematical models [11]. Then, the faults are analyzed using a variety of analytical methods.

Taking the research object as an example, in the study of fault diagnosis of other complex nonlinear systems such as aircraft hydraulic systems, Jianhua Zhao [12] et al. created the drop shock friction equation for the failure mode of single-degree-of-freedom bearing systems, providing a theoretical basis for fault prevention and diagnosis of

 doi:10.20944/preprints202207.0247.v1

Magnetic-liquid double suspension bearings (MLDSB). Cordelia Mattuvarkuzhali Ezhilarasu [13] et al. created an electrical power system (EPS) diagnostic algorithm to detect and isolate line replaceable units (LRU) problems and their primary causes. Kenan Shen [14] et al. suggested a new one-dimensional multichannel convolutional neural network (1DMCCNN) for diagnosing failure scenarios to improve aviation hydraulic system reliability and safety. Zhang Lixia [15] et al. proved the variation law of resolved redundancy relations under different faults by simulation tests, and highlighted the feasibility of fault diagnosis and isolation (FDI) design and implementation of hybrid systems utilizing GARRs approach. Ming Yu [16] et al. described complicated systems subject to parameter uncertainty and compound faults using a diagnostic bond graph.

Taking the power bond graph modeling method as an example, Wang Jinxin [17] et al. constructed a diesel engine lubrication system dynamics model and translated it into a temporal causal diagram for fault diagnostics, proving multi-fault decoupling in lubrication systems effective. Wang Junnian[18,19] et al. suggested a method to obtain the analytic redundancy equation based on the bond graph model and the resultant temporal causal diagram. The experimental results proved that the analytic redundancy equation derived by this method could be used for fault diagnosis. Zhang Xiaokang [20] et al. used the bond graph approach to create the system state equations and performed simulation calculations on the 20-sim simulation platform to get the dynamic spray pressure characteristics under different pressure settings. K. Medjaher [21] et al. devised an algorithm for calculating real-time residuals using online process variable measurements. Wei Chunling [22] et al. employed the sequential probability ratio test (SPRT) to monitor online residual abnormalities in quantitative system fault identification and isolation. M.A. Djeziri [23] et al. proposed a robust defect detection and isolation method based on a bonded graph using the same tool to synthesis nonlinear models, structural analysis, residuals with adaptive threshold generation, and residual sensitivity analysis.

Taking the fault analysis methods ARRs and GARRs as an example, in order to generate ARRs efficiently, Du Minjie [24] et al. constructed a hypothetical signature matrix (HSM), which they subsequently solved using the binary particle swarm optimization (BPSO) algorithm. A fault diagnosability evaluation approach based on graph theory was proposed by Liu Wenjing et al. [25,26], and the efficacy of the proposed method was confirmed using mathematical simulation data based on the addition of weighted directed graphs. And investigated the issue of satellite attitude control system fault diagnosability analysis and fault diagnosis based on analytical redundancy relation (ARR). A failure diagnosis approach for wind turbines was suggested by Hector Sanchez [27,28] et al. by fusing the ARR and the interval observers. Additionally, the advanced wind turbine benchmark failure diagnosis problem will be solved in a restricted context while taking uncertainty factors into account by combining ARR and observers. When studying a linear bond graph with information bonds, K. SIA [29] et al. suggested a new structural method for producing analytical redundancy relations from linear and linear bond graphs that is appropriate for large-scale systems.

Figure 1 depicts the precise steps and methodology of this work, and the literature [30] is cited for the fundamental ideas. During modeling, it is vitally crucial to collect and analyze the physical characteristics of each component. The diagnostic bond graph (BG) of the R/E system is obtained by injecting faults, virtual sensors, and reverse causality, based on which the ARRs of the system can be obtained. System fault status control is accomplished using logical Boolean variable. To identify the fault, the residuals determined by GARRs is compared with the thresholds. If the residuals are within the threshold range, no fault is discovered; if the residuals are outside the threshold range, a fault is detected.

Preprints (www.preprints.org) | NOT PEER-REVIEWED | Posted: 18 July 2022 doi:10.20944/preprints202207.0247.v1

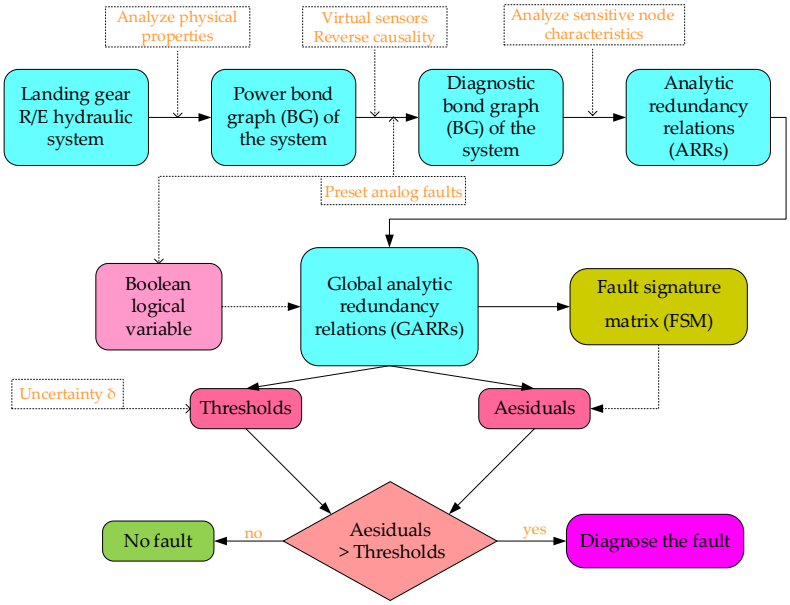

Figure 1. Research structure.

2. Modeling of landing R/E hydraulic system based on power bond graph

2.1. Modeling of faultless system

Figure 2 depicts the basic layout of the landing gear R/E hydraulic system. Both an EDP (engine-driven pump) and an EMDP (electric motor-driven pump) are used to power the system [31]. In the left and right main landing gear (MLG) and nose landing gear (NLG), the hydraulic components of the landing gear selection valve distribute high pressure hydraulic oil to the R/E hydraulic components. The overflow valve, check valve, throttle valve, and hydraulic safety components are not represented in the diagram because the left and right main landing gears are symmetrically almost identical. Next, by examining each component's physical makeup, the system's components are modeled individually using the power bond graph modeling technique, where the generalized potential variable e in the hydraulic system refers to the pressure p, and the generalized flow variable f in the hydraulic system refers to the flow rate Q.

(1) Hydraulic source.

EDP and EMDP, with filters, check valves, overflow valves, and other accessories make up the hydraulic source. Since the EDP physically consists of an axial piston type variable flow piston pump that transforms engine mechanical energy into hydraulic energy, a translator TF can be used to represent it, as shown in Figure 3 (a). EMDP is a single-stage hydraulic centrifugal pump, suitable for modeling the gyrator GY, as shown in Figure 3(b). Overflow valves are used to maintain a relatively constant gauge pressure in front of them and to drain excess hydraulic oil away from them, as seen in Figure 3(c). Despite its role as an auxiliary hydraulic source for stabilizing the hydraulic pump and transmitting speed over a range of pressures, the accumulator will be removed from the failure analysis without modeling because it complicates failure analysis. For information on the meaning of the associated parameters in the figure, refer to Table S1.

As shown in Figure 3(d), the overflow valve, EDP, and EMDP components are combined into a single simplified model. The parameters are defined in Table S1. This is done because the number of bonds in each component is very considerable, which will make the subsequent failure analysis very complicated. All models must satisfy the fundamental requirements of equal pressure at the common potential node (0-node) and equal flow at the common flow node (1-node). State and variation quantities of pressure are located on the half-tip arrow's side, whereas state and variation quantities of flow are located on the side without the tip. The signal bond is indicated by the entire arrow, which denotes

Preprints (www.preprints.org) | NOT PEER-REVIEWED | Posted: 18 July 2022 doi:10.20944/preprints202207.0247.v1

that there is a functional connection between the parametric parameters at its two end-points.

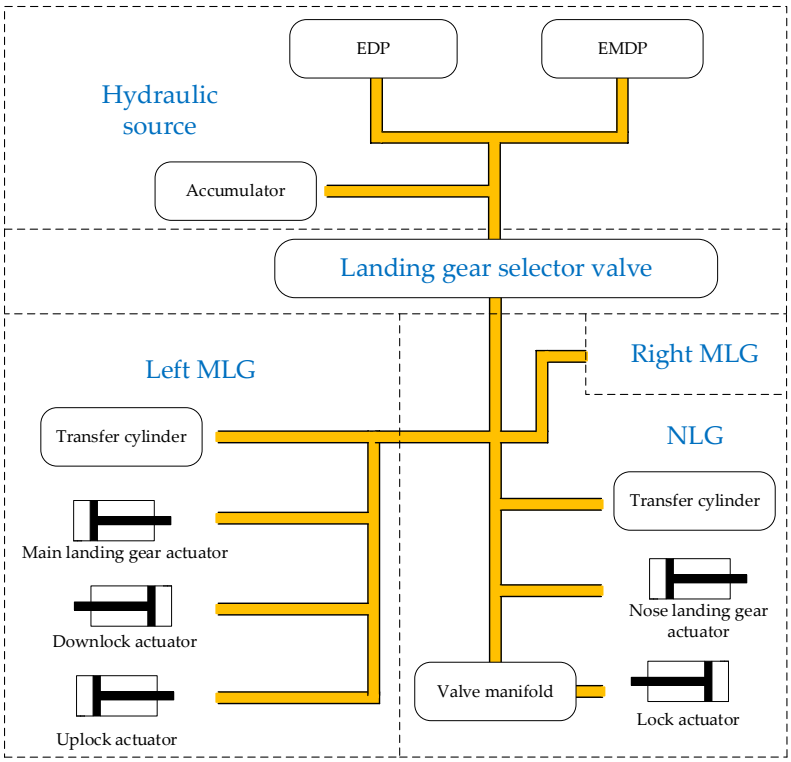

Figure 2. Basic structure of landing gear R/E hydraulic system.

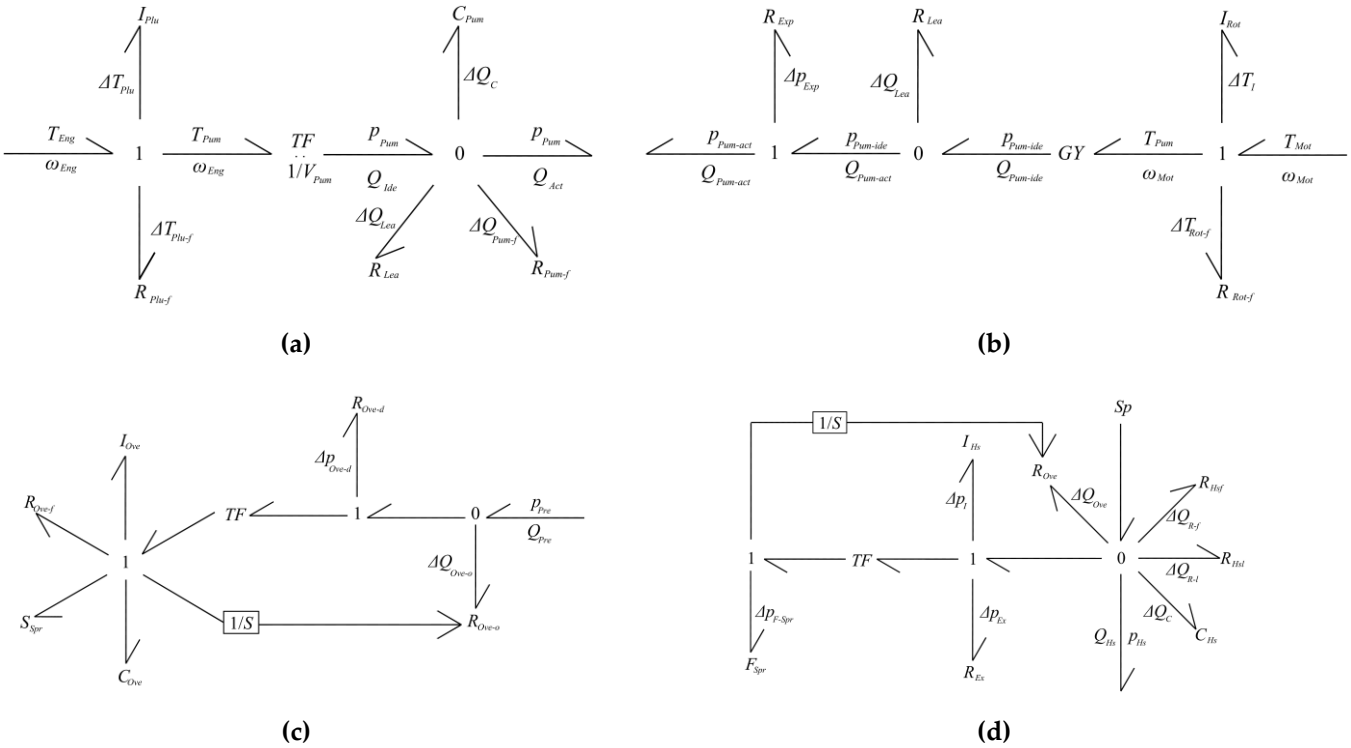

Figure 3. Bond graph model of hydraulic source: (**a**) EDP; (**b**) EMDP; (**c**) Overflow valve; (**d**) Hydraulic source simplified model.

Preprints (www.preprints.org) | NOT PEER-REVIEWED | Posted: 18 July 2022 doi:10.20944/preprints202207.0247.v1

(2) Landing gear selector valve.

Figure 4(a) illustrates the physical essence of the landing gear selector valve, which is a Y-type, 3-position 4-way solenoid directional valve. The P-port closed A, B, and T ports connected, the floating piston, ability to move in response to external forces, and hydraulic pump does not unload are the characteristics that define its median function. Figures 4(b) (c) (d) depict the landing gear selector valve's neutral, left, and right operational states. Figure 5 depicts the bond graph model of the landing gear selector valve.

Port P is the supply port, Port T is the return port, and Ports A and B are connected to the subsequent pipes. 4 paths (PA, PB, AT, BT) are formed by the valve body and spool's relative positions, and the corresponding fluid resistance are R_{PA}, R_{PB}, R_{AT}, and R_{BT}. Neutral, left, and right working states of the landing gear selector valve correspond to the following meanings [32]:

1) Neutral: Now that the high pressure source P port is disconnected from the system, the A and B ports are attached to the return port T. Hydraulic oil returns to the tank through the hydraulic resistance R_{AT} of the AT path and the hydraulic resistance R_{BT} of the BT path, respectively. At this time, liquid resistance R_{PA} and R_{PB} are not considered.

2) Left: Port A is connected to the return port T, whereas port B is connected to the high pressure source port P. Through R_{PB} of the PB path, high pressure hydraulic oil exits from port B. Through R_{AT} of the path AT, hydraulic oil from the return line flows back to tank. Liquid resistance R_{PA} and R_{BT} are not taken into consideration at this time.

3) Right : Port B is connected to the return port T, whereas port A is connected to the high pressure source port P. Through R_{PA} of the PA path, high pressure hydraulic oil exits from port A. Through R_{BT} of the path BT, hydraulic oil from the return line flows back to tank. Liquid resistance R_{PB} and R_{AT} are not taken into consideration at this time.

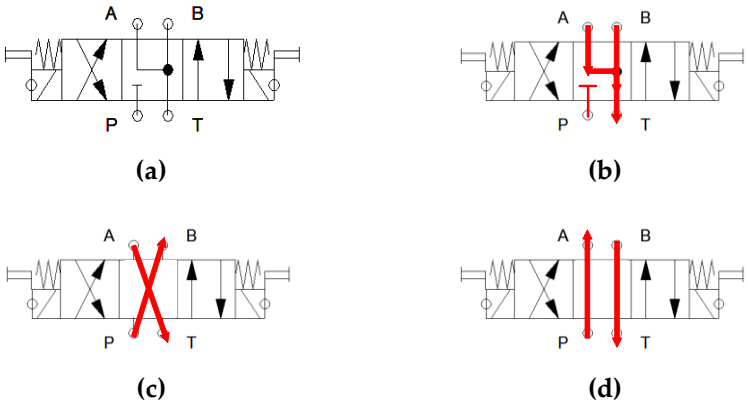

Figure 4. Landing gear selector valve and its working state: (**a**) Landing gear selector valve; (**b**) Neutral function; (**c**) Left position status; (**d**) Right position status.

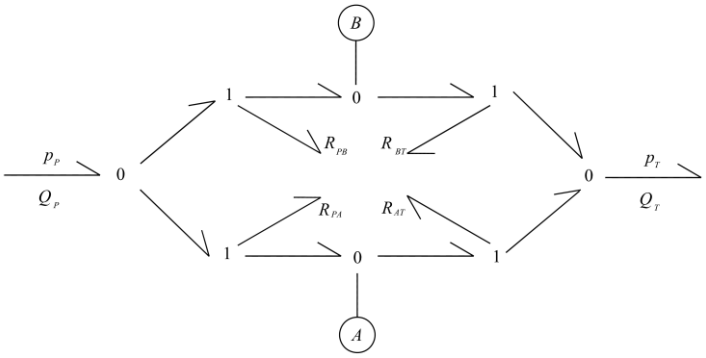

Figure 5. Landing gear selector valve bond graph.

Preprints (www.preprints.org) | NOT PEER-REVIEWED | Posted: 18 July 2022 doi:10.20944/preprints202207.0247.v1

(3) Actuator and transfer cylinder.

Actuator is a component used to reciprocate linear motion in a hydraulic system by converting hydraulic energy into mechanical energy. Landing gear R/E hydraulics include the main landing gear actuator, downlock actuator, uplock actuator, and nose landing gear actuator and lock actuator [33]. Since all actuators have the exact same physical characteristics, only one modeling is needed. The model is depicted in Figure 6, and Table S2 lists the definitions of the parameters for the actuator and transfer cylinder.

Transfer cylinder, which controls the operating sequence hydraulically, is connected in parallel with the delayed cylinder. The transfer cylinder is connected in parallel with the R/E actuator in the landing gear R/E system, delaying the R/E actuator's activation and guaranteeing that the lock actuator acts first and the R/E actuator operates second. Figure 7(a) displays the fundamental schematic diagram, and Figure 7(b) displays the bond graph model. Table S2 displays the definitions of the parameters in the diagram.

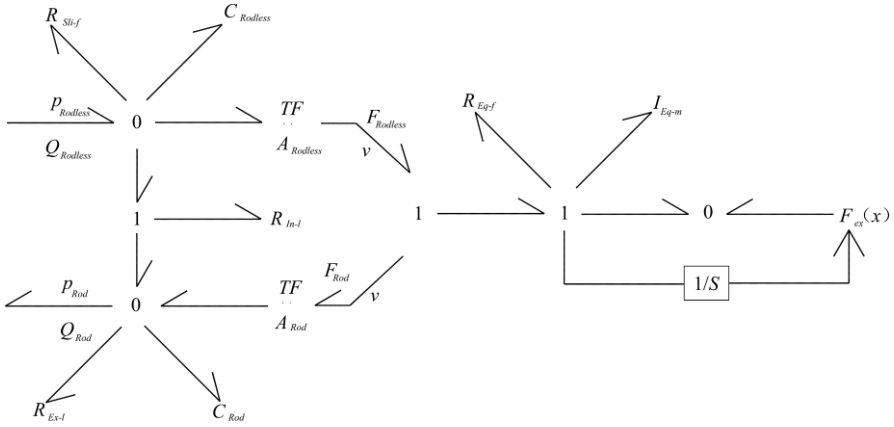

Figure 6. Actuator bond graph.

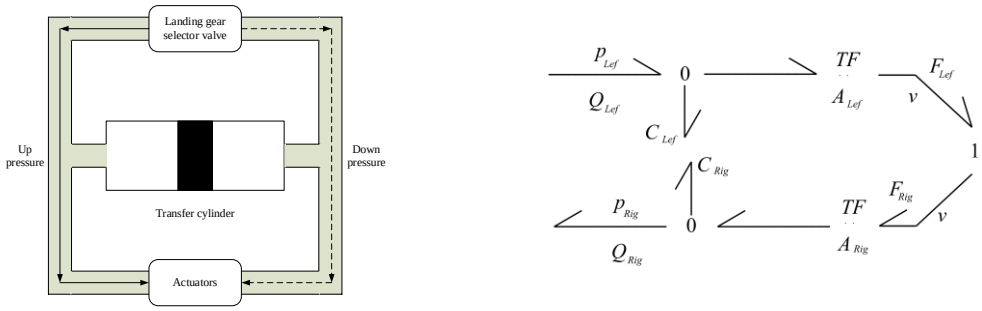

(a) **(b)**

Figure 7. Transfer cylinder: (**a**) Basic schematic diagram; (**b**) Bond graph.

(4) Check valve, throttle valve, filter and pipe elbow.

Check valves are used to limit the flow of hydraulic fluid so that it can only go forward and not backward. It is installed at the pump outlet in the hydraulic system of the aircraft to guard against damage to the hydraulic pump caused by an abrupt rise in reverse pressure. Purity and quality of hydraulic oil are enhanced by the filter's ability to capture solid contaminants. Flow and pressure are controlled by the throttle valve; when there is a known difference in valve pressure, flow changes are influenced by the size of the opening. Hydraulic pipeline can not be all straight, there will inevitably be elbow structure, hydraulic oil impact elbow will cause pressure loss. The bond graph model of the above components is shown in Figure 8, and the meanings of the corresponding parameters are shown in Table S3.

Preprints (www.preprints.org) | NOT PEER-REVIEWED | Posted: 18 July 2022 doi:10.20944/preprints202207.0247.v1

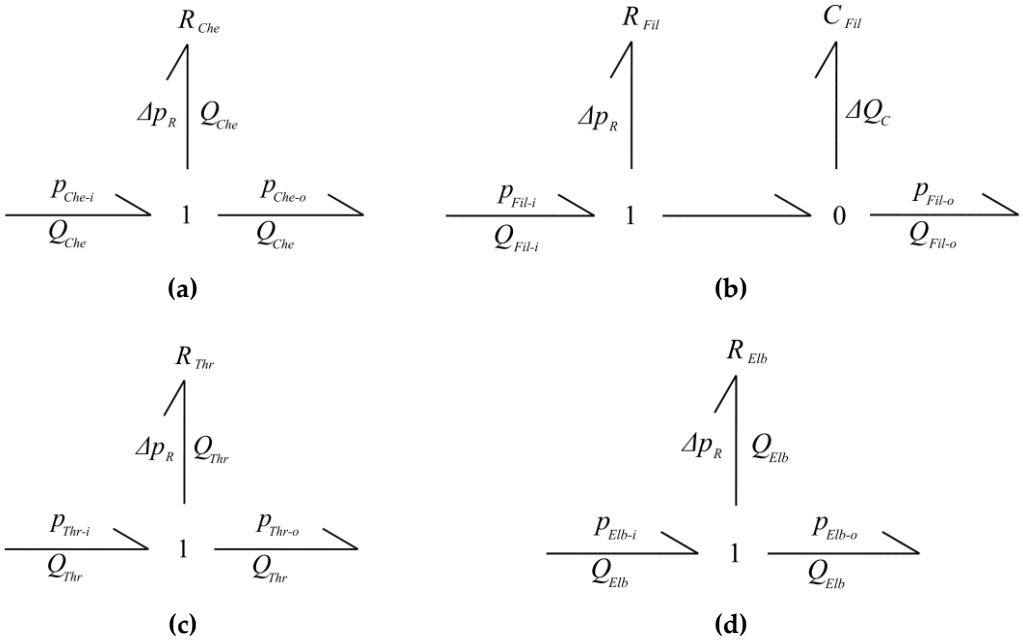

Figure 8. Component bond graph: (**a**) Check valve; (**b**) Filter; (**c**) Throttle valve; (**d**) Elbow.

(5) Hydraulic pipe and pipe elbow.

Pipe serves as the hydraulic oil's transportation path, and the hydraulic pump transfers hydraulic energy from the reservoir to each actuator via the pipe to make the system function. Divide the long pipeline into n short pipeline units as part of the modeling process [34], and the units are numbered from 1 to n. The angle of the hydraulic pipeline layout is not taken into consideration at this time because the same kind of fluid effect of various units is assumed to be the same. Figure 9 depicts the modeling, and Table S4 provides the references used to create the figure.

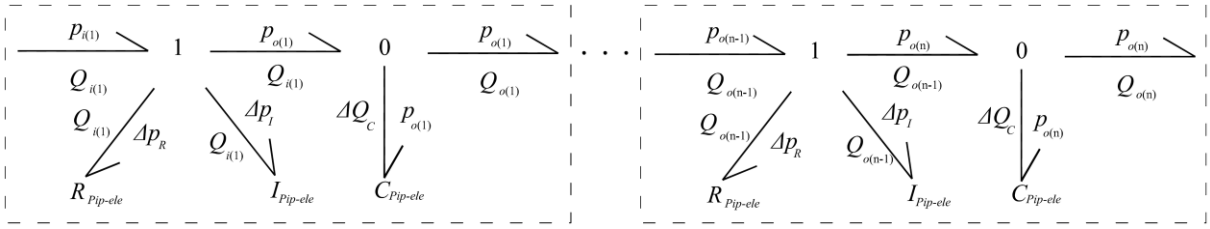

Figure 9. Hydraulic pipe bond graph.

Although there are several actuators in the system, by only using the R/E actuator as terminals, the analysis is made simpler. The landing gear R/E hydraulic system bond graph model is created by connecting all of the aforementioned component structures, assigning causality to all connections, numbering those bonds, and numbering all of the nodes. Figure 10 shows the result. According to the literature [35], the following guidelines were used to determine the cause:

1) There is a sole causal relationship between the potential source and the flow source, with the potential source's causality stroke on the side closest to the tip and the flow source's causality stroke on the side farther from the tip.
2) Both inertial and capacitive elements have precedence for defining integral causality, but the causality of the inertial element is on the side closest to the tip, whereas the causality of the capacitive element is on the side farthest from the tip.
3) The resistive component prioritizes admittance type causality; the causality stroke is on the tip side, but coordination with other bond graph parts must be taken into

Preprints (www.preprints.org) | NOT PEER-REVIEWED | Posted: 18 July 2022 doi:10.20944/preprints202207.0247.v1

account throughout the designation process, and the causality is extended in the direction of flow at the node.

Each bond and node is numbered according to the following principles:

1) Starting from number *1*, each bond is numbered in turn, counterclockwise, centered on the node, and the signal bonds are not numbered.
2) Starting from number *(1)*, each node is numbered according to the direction of energy flow, and the converter *TF* node is not numbered.

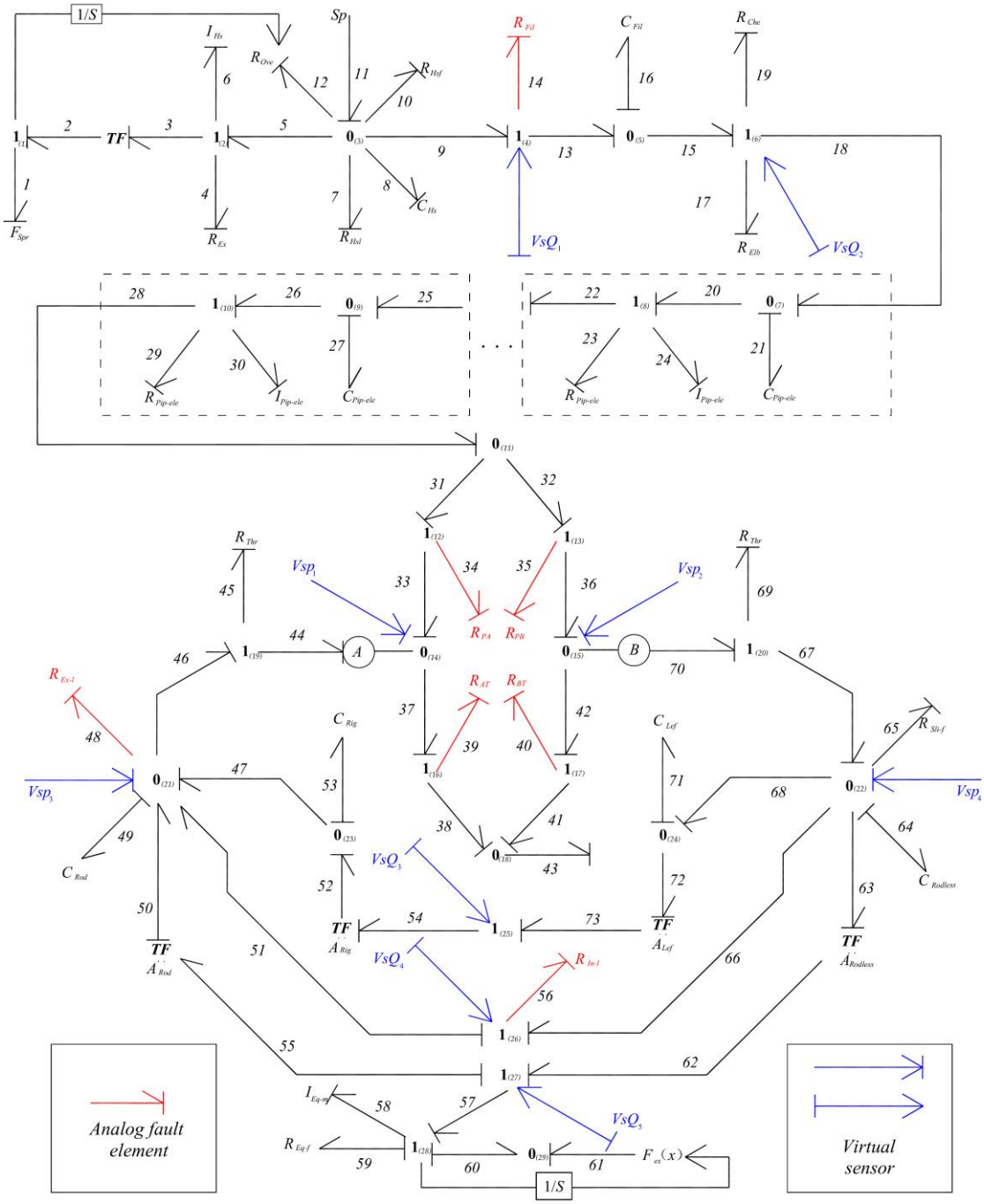

Figure 10. Bond graph of landing gear R/E hydraulic system.

2.2. Modeling of multi fault system and placement of virtual sensors

Since there is no such thing as an absolutely perfect system without degradation, the fault-free modeling of the system takes into account a wide variety of potential leaky fluid

Preprints (www.preprints.org) | NOT PEER-REVIEWED | Posted: 18 July 2022 doi:10.20944/preprints202207.0247.v1

resistances, blocked fluid resistances, stuck fluid resistances, etc. In order to simulate and inject faults, only the pertinent resistive element parameters need to be changed.

There are numerous ways to categorize defects, including minor, general, serious, and deadly faults based on the degree of degradation of faults, and abrupt and progressive faults based on the degree of progression of faults. A, B, C, and D are the four typical defects examined in this study. Table 1 lists the designed fault types. Define the Boolean logic variable β that will be used to describe the system's operational state:

$$\beta = [\mathrm{A,B,C,D}] \quad (\mathrm{A/B/C/D} = 0 \ or \ 1) \tag{1}$$

For example, $\beta = [1,0,0,0]$ means that only type A faults exist and no type B/C/D faults exist.

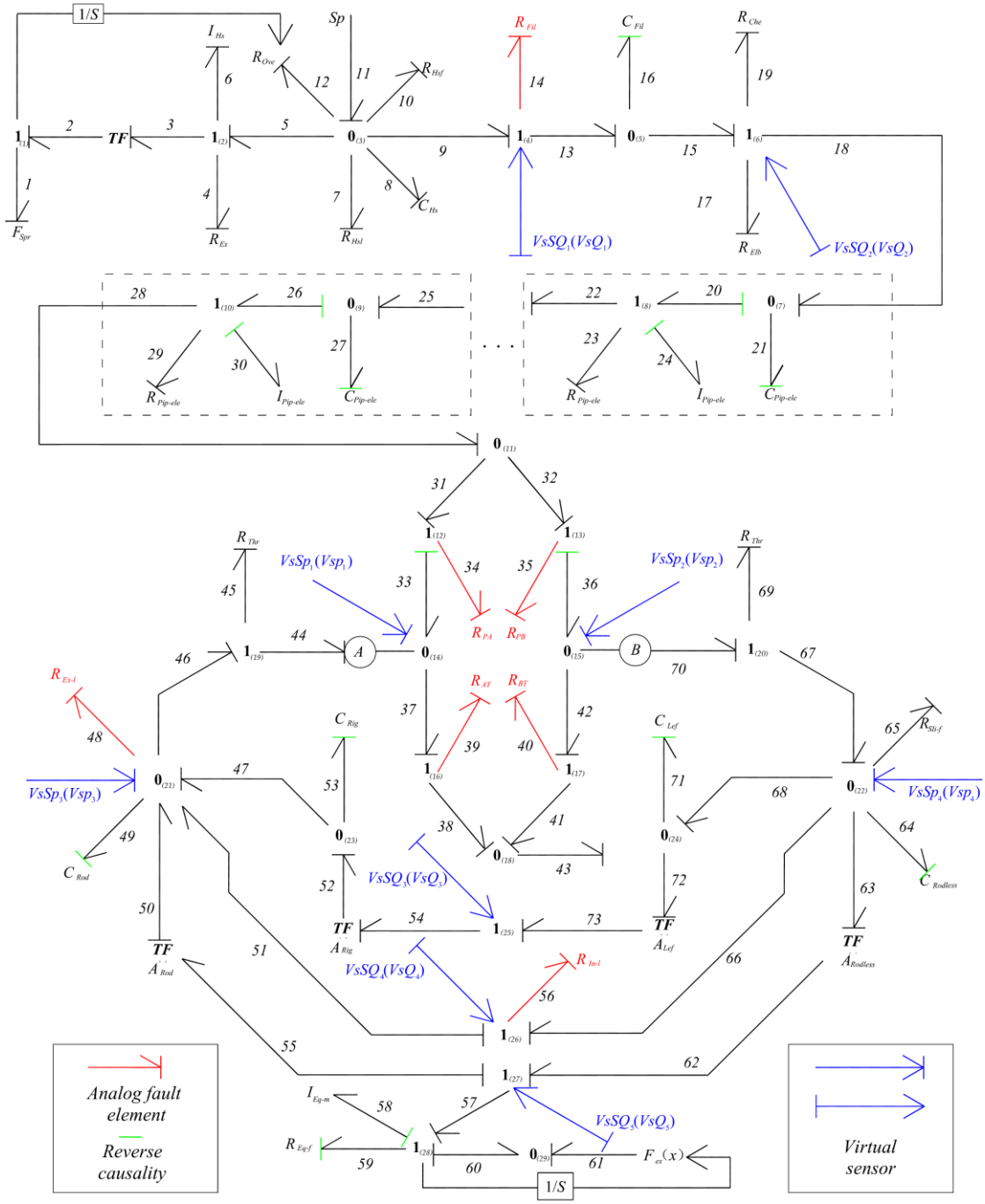

Figure 11. Diagnostic bond graph of landing gear R/E hydraulic system.

Preprints (www.preprints.org) | NOT PEER-REVIEWED | Posted: 18 July 2022 doi:10.20944/preprints202207.0247.v1

Table 1. Fault type and corresponding parameters.

Fault type number	Components involved	Meaning
A	R_{Fil}	Filter clogged
B	R_{Ex-l}	External leakage of actuator
C	R_{In-l}	Internal leakage of actuator
D	R_{PA} R_{PB} R_{AT} R_{BT}	Landing gear selector valve stuck

In accordance with the literature [36], the pre-defined fault nodes and the nodes where multiple bonds converge in the system are chosen as the virtual sensor placement locations. To detect the pressure signal, the pressure sensor is placed at the common potential node (0-node), and to detect the flow signal, the flow sensor is placed at the common flow node (1-node). Table 2 displays the correspondence between the sensor's and GRR. Figure 11 depicts the system's diagnostic bond graph.

Table 2. Set virtual sensors and corresponding GARRs.

Flow virtual sensor	Pressure virtual sensor
$VsQ_1 : \mathrm{GARR}_1$	$Vsp_1 : \mathrm{GARR}_3$
$VsQ_2 : \mathrm{GARR}_2$	$Vsp_2 : \mathrm{GARR}_4$
$VsQ_3 : \mathrm{GARR}_7$	$Vsp_3 : \mathrm{GARR}_5$
$VsQ_4 : \mathrm{GARR}_8$	$Vsp_4 : \mathrm{GARR}_6$
$VsQ_5 : \mathrm{GARR}_9$	

3. Global analytic redundancy relations and fault signature matrix

In bond graph model-based fault diagnostics, the term "analytical redundancy relation" (ARR) refers to a constraint relationship obtained from a system model based on the rule of energy conservation. As a rule of thumb, the number of analytical redundancy relations generated from the system is equal to that of virtual sensors. These relations are known as analytic redundancy relations (ARRs), and they become global analytic redundancy relations (GARRs) when the Boolean logic variable β is taken into account:

$$\begin{cases} \mathrm{ARR}_i = f_i(k_i, \theta_i) \qquad i = 1, \cdots, n \\ \mathrm{GARR}_i = \mathrm{ARR}_i(\beta) \\ \mathrm{GARRs} = [\mathrm{GARR}_1, \mathrm{GARR}_2, \cdots, \mathrm{GARR}_n] \end{cases} \tag{2}$$

where i is the number of the GARR, k_i is the system variable, θ_i is the system parameter, and f_i is a function of the k_i and θ_i.

To estimate GARRs using the bond graph model, three approaches are commonly used: causal path coverage, causal inversion, and temporal causal graph methods [37]. The temporal causal graph method is not impacted by the causal configuration, and the causal path coverage method is very effective. However, due to the complexity of the model in this study, the causal inversion method, which only requires analyzing the nodes connected to the virtual sensors, can be used to obtain GARRs most easily.

In both the causal inversion approach and the causal path overlay method, GARRs are derived from the intrinsic equations of the nodes, but the causal inversion approach is better because only one node is connected to the virtual sensor. In order to construct GARRs without deviating from the bonding diagram's causal laws, the causal delineation of nodes must be adjusted. Figure 11 displays the diagnostic bonding diagram following causative inversion. The principal equation of the basic form of the causal relationship for all types of components is shown in Table 3, where the generalized potential variable corresponds to pressure p and the generalized flow variable corresponds to flow rate Q, φ indicates the functional relationship that exists.

Preprints (www.preprints.org) | NOT PEER-REVIEWED | Posted: 18 July 2022 doi:10.20944/preprints202207.0247.v1

Table 3. The basic principal construct equation of causality.

Element type	Causal relationship type		Constitutive equations
Potential source	Unique type:	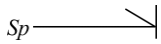	$Q=0, p$
Stream source	Unique type:	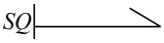	$p=0, Q$
Capacitive element	Integral type:	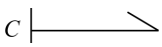	$p(t)=\varphi_C(\int Q(t)dt)$
	Differential type:	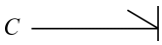	$Q(t)=\frac{d}{dt}\varphi_C^{-1}(p(t))$
Inertial element	Integral type:	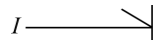	$Q(t)=\varphi_I(\int p(t)dt)$
	Differential type:	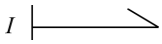	$Q(t)=\frac{d}{dt}\varphi_I^{-1}(p(t))$
Resistive element	Impedance type:	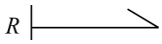	$p(t)=\varphi_R(Q(t))$
	Admittance type:	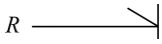	$Q(t)=\varphi_R^{-1}(p(t))$

GARR at the co-potential node (0-node) can be summarized as " Same potential variable divides the flow variable ", and at the co-flow node (1-node) can be summarized as " Same flow variable divides the potential variable ":

$$0-\text{node}:\begin{cases} p_1=p_2=p_3=\cdots p_n \\ \text{GARR}=\sum_{i=1}^{n}\alpha_i Q_i \end{cases} \quad i=1,2,3,\cdots n \tag{3}$$

$$1-\text{node}:\begin{cases} Q_1=Q_2=Q_3=\cdots Q_n \\ \text{GARR}=\sum_{i=1}^{n}\alpha_i p_i \end{cases} \quad i=1,2,3,\cdots n \tag{4}$$

where n is the node's bond excluding the virtual sensor; α_i is the power flow coefficient, for the bond with the half-arrow pointing to the node $\alpha_i=1$ and for the bond with the half-arrow departing from the node $\alpha_i=-1$ [38]. Then, GARRs are written.

GARR_1 for node $1_{(4)}$:

$$1_{(4)}-\text{node}:\begin{cases} Q_9=Q_{13}=Q_{14} \\ \text{GARR}_1=p_9-p_{13}-p_{14}=0 \end{cases} \tag{5}$$

$$\begin{cases} p_9=p_{11}=Sp=p_{12}=R_{Ove}Q_{Ove} \\ p_{13}=p_{16}=\frac{1}{C_{Fil}}\int Q_{16}dt=\frac{1}{C_{Fil}}\int(Q_{13}-Q_{15})dt=\frac{1}{C_{Fil}}\int(VsSQ_1-VsSQ_2)dt \\ p_{14}=\text{AR}_{Fil}VsSQ_1 \end{cases} \tag{6}$$

$$\text{GARR}_1=Sp-\text{AR}_{Fil}VsSQ_1-\frac{1}{C_{Fil}}\int(VsSQ_1-VsSQ_2)dt \tag{7}$$

GARR_2 for node $1_{(6)}$:

$$1_{(6)}-\text{node}:\begin{cases} Q_{15}=Q_{17}=Q_{18}=Q_{19} \\ \text{GARR}_2=p_{15}-p_{17}-p_{18}-p_{19}=0 \end{cases} \tag{8}$$

Preprints (www.preprints.org) | NOT PEER-REVIEWED | Posted: 18 July 2022 doi:10.20944/preprints202207.0247.v1

$$\begin{cases} p_{15} = p_{16} = \dfrac{1}{C_{Fil}}\int (VsSQ_1 - VsSQ_2)dt \\ p_{17} = R_{Elb}VsSQ_2 \\ Q_{21} = Q_{18} - Q_{20} = (VsSQ_2 - \dfrac{\mathrm{D}VsSp_1}{R_{PA}} - \dfrac{\mathrm{D}VsSp_2}{R_{PB}}) \\ p_{18} = p_{21} = \dfrac{1}{nC_{Pip-ele}}\int Q_{21}dt = \dfrac{1}{nC_{Pip-ele}}\int (VsSQ_2 - \dfrac{\mathrm{D}VsSp_1}{R_{PA}} - \dfrac{\mathrm{D}VsSp_2}{R_{PB}})dt \\ p_{19} = R_{Che}VsSQ_2 \end{cases} \tag{9}$$

$$\mathrm{GARR}_2 = \frac{1}{C_{Fil}}\int (VsSQ_1 - VsSQ_2)dt - \frac{1}{nC_{Pip-ele}}\int (VsSQ_2 - \frac{\mathrm{D}VsSp_1}{R_{PA}} - \frac{\mathrm{D}VsSp_2}{R_{PB}})dt - (R_{Elb} + R_{Che})VsSQ_2 \tag{10}$$

GARR_3 for node $0_{(14)}$:

$$0_{(14)} - \text{node:} \begin{cases} p_{33} = p_{37} = p_{44} \\ \mathrm{GARR}_3 = Q_{33} + Q_{44} - Q_{37} = 0 \end{cases} \tag{11}$$

$$\begin{cases} p_{28} = \dfrac{1}{C_{Fil}}\int (VsSQ_1 - VsSQ_2)dt - (R_{Elb} + R_{Che})VsSQ_2 \\ Q_{33} = Q_{34} = \dfrac{\mathrm{D}p_{34}}{R_{PA}} = \dfrac{\mathrm{D}(p_{31} - p_{33})}{R_{PA}} = \dfrac{\mathrm{D}(p_{28} - VsSp_1)}{R_{PA}} = \dfrac{\mathrm{D}[\dfrac{1}{C_{Fil}}\int (VsSQ_1 - VsSQ_2)dt - (R_{Elb} + R_{Che})VsSQ_2 - VsSp_1]}{R_{PA}} \\ Q_{44} = Q_{45} = \dfrac{p_{45}}{R_{Thr}} = \dfrac{p_{46} - p_{44}}{R_{Thr}} = \dfrac{VsSp_3 - VsSp_1}{R_{Thr}} \\ Q_{37} = Q_{39} = \dfrac{\mathrm{D}p_{39}}{R_{AT}} = \dfrac{\mathrm{D}(p_{37} - p_{38})}{R_{AT}} = \dfrac{\mathrm{D}(VsSp_1 - p_T)}{R_{AT}} \end{cases} \tag{12}$$

$$\mathrm{GARR}_3 = \frac{\mathrm{D}[\frac{1}{C_{Fil}}\int (VsSQ_1 - VsSQ_2)dt - (R_{Elb} + R_{Che})VsSQ_2 - VsSp_1]}{R_{PA}} + \frac{VsSp_3 - VsSp_1}{R_{Thr}} - \frac{\mathrm{D}(VsSp_1 - p_T)}{R_{AT}} \tag{13}$$

GARR_4 for node $0_{(15)}$:

$$0_{(15)} - \text{node:} \begin{cases} p_{36} = p_{42} = p_{70} \\ \mathrm{GARR}_4 = Q_{36} - Q_{42} - Q_{70} = 0 \end{cases} \tag{14}$$

$$\begin{cases} p_{28} = \dfrac{1}{C_{Fil}}\int (VsSQ_1 - VsSQ_2)dt - (R_{Elb} + R_{Che})VsSQ_2 \\ Q_{36} = Q_{35} = \dfrac{\mathrm{D}p_{35}}{R_{PB}} = \dfrac{\mathrm{D}(p_{32} - p_{36})}{R_{PB}} = \dfrac{\mathrm{D}(p_{28} - VsSp_2)}{R_{PB}} = \dfrac{\mathrm{D}[\dfrac{1}{C_{Fil}}\int (VsSQ_1 - VsSQ_2)dt - (R_{Elb} + R_{Che})VsSQ_2 - VsSp_2]}{R_{PB}} \\ Q_{42} = Q_{40} = \dfrac{\mathrm{D}p_{40}}{R_{BT}} = \dfrac{\mathrm{D}[p_{42} - p_{41}]}{R_{BT}} = \dfrac{\mathrm{D}[VsSp_2 - p_T]}{R_{BT}} \\ Q_{70} = Q_{69} = \dfrac{p_{69}}{R_{Thr}} = \dfrac{p_{70} - p_{67}}{R_{Thr}} = \dfrac{VsSp_2 - VsSp_4}{R_{Thr}} \end{cases} \tag{15}$$

Preprints (www.preprints.org) | NOT PEER-REVIEWED | Posted: 18 July 2022 doi:10.20944/preprints202207.0247.v1

$$\mathrm{GARR}_4=\frac{\mathrm{D}[\frac{1}{C_{Fil}}\int(VsSQ_1-VsSQ_2)dt-(R_{Elb}+R_{Che})VsSQ_2-VsSp_2]}{R_{PB}}-\frac{VsSp_2-VsSp_4}{R_{Thr}}-\frac{\mathrm{D}(VsSp_2-p_T)}{R_{BT}} \tag{16}$$

GARR_5 for node $0_{(21)}$:

$$0_{(21)}-\mathrm{node}:\begin{cases}p_{46}=p_{47}=p_{48}=p_{49}=p_{50}=p_{51}\\ \mathrm{GARR}_5=Q_{47}+Q_{50}+Q_{51}-Q_{46}-Q_{48}-Q_{49}=0\end{cases} \tag{17}$$

$$\begin{cases}Q_{47}=Q_{52}-Q_{53}=\dfrac{VsSQ_3}{A_{Rig}}-C_{Rig}\dfrac{d(VsSp_3)}{dt}\\ Q_{50}=\dfrac{Q_{55}}{A_{Rod}}=\dfrac{VsSQ_5}{A_{Rod}}\\ Q_{51}=VsSQ_4\\ Q_{46}=Q_{45}=\dfrac{p_{45}}{R_{Thr}}=\dfrac{VsSp_3-VsSp_1}{R_{Thr}}\\ Q_{48}=\dfrac{\mathrm{B}VsSp_3}{R_{Ex-l}}\\ Q_{49}=C_{Rod}\dfrac{d(VsSp_3)}{dt}\end{cases} \tag{18}$$

$$\mathrm{GARR}_5=\frac{VsSQ_3}{A_{Rig}}+\frac{VsSQ_5}{A_{Rod}}-\frac{VsSp_3-VsSp_1}{R_{Thr}}-\frac{\mathrm{B}VsSp_3}{R_{Ex-l}}+VsSQ_4-(C_{Rig}+C_{Rod})\frac{d(VsSp_3)}{dt} \tag{19}$$

GARR_6 for node $0_{(22)}$:

$$0_{(22)}-\mathrm{node}:\begin{cases}p_{63}=p_{64}=p_{65}=p_{66}=p_{67}=p_{68}\\ \mathrm{GARR}_6=Q_{67}-Q_{63}-Q_{64}-Q_{65}-Q_{66}-Q_{68}=0\end{cases} \tag{20}$$

$$\begin{cases}Q_{67}=Q_{69}=\dfrac{p_{69}}{R_{Thr}}=\dfrac{VsSp_2-VsSp_4}{R_{Thr}}\\ Q_{63}=A_{Rodless}Q_{62}=A_{Rodless}VsSQ_5\\ Q_{64}=C_{Rodless}\dfrac{d(VsSp_4)}{dt}\\ Q_{65}=\dfrac{VsSp_4}{R_{Sli-f}}\\ Q_{66}=VsSQ_4\\ Q_{68}=Q_{71}+Q_{72}=C_{Lef}\dfrac{d(VsSp_4)}{dt}+A_{Lef}VsSQ_3\end{cases} \tag{21}$$

$$\mathrm{GARR}_6=\frac{VsSp_2-VsSp_4}{R_{Thr}}-\frac{VsSp_4}{R_{Sli-f}}-A_{Rodless}VsSQ_5-A_{Lef}VsSQ_3-VsSQ_4-(C_{Rodless}+C_{Lef})\frac{d(VsSp_4)}{dt} \tag{22}$$

GARR_7 for node $1_{(25)}$:

$$1_{(25)}-\mathrm{node}:\begin{cases}Q_{54}=Q_{73}\\ \mathrm{GARR}_7=p_{73}-p_{54}=0\end{cases} \tag{23}$$

Preprints (www.preprints.org) | NOT PEER-REVIEWED | Posted: 18 July 2022 doi:10.20944/preprints202207.0247.v1

$$\begin{cases} p_{73} = A_{Lef}\, p_{72} = A_{Lef} VsSp_4 \\ p_{54} = \dfrac{p_{52}}{A_{Rig}} = \dfrac{VsSp_3}{A_{Rig}} \end{cases} \tag{24}$$

$$\mathrm{GARR}_7 = A_{Lef} VsSp_4 - \frac{VsSp_3}{A_{Rig}} \tag{25}$$

GARR_8 for node $1_{(26)}$:

$$1_{(26)} - \mathrm{node}: \begin{cases} Q_{51} = Q_{56} = Q_{66} \\ \mathrm{GARR}_8 = p_{66} - p_{51} - p_{56} = 0 \end{cases} \tag{26}$$

$$\begin{cases} p_{66} = VsSp_4 \\ p_{51} = VsSp_3 \\ p_{56} = \mathrm{C}R_{In-l} VsSQ_4 \end{cases} \tag{27}$$

$$\mathrm{GARR}_8 = VsSp_4 - VsSp_3 - \mathrm{C}R_{In-l} VsSQ_4 \tag{28}$$

GARR_9 for node $1_{(27)}$:

$$1_{(27)} - \mathrm{node}: \begin{cases} Q_{62} = Q_{55} = Q_{57} \\ \mathrm{GARR}_9 = p_{62} - p_{55} - p_{57} = 0 \end{cases} \tag{29}$$

$$\begin{cases} p_{62} = A_{Rodless}\, p_{63} = A_{Rodless} VsSp_4 \\ p_{55} = \dfrac{p_{50}}{A_{Rod}} = \dfrac{VsSp_3}{A_{Rod}} \\ p_{57} = p_{58} + p_{59} + p_{60} = I_{Eq-m} \dfrac{dVsSQ_5}{dt} + R_{Eq-f} VsSQ_5 + F_{ex}(x) \end{cases} \tag{30}$$

$$\mathrm{GARR}_9 = A_{Rodless} VsSp_4 - \frac{VsSp_3}{A_{Rod}} - I_{Eq-m} \frac{dVsSQ_5}{dt} - R_{Eq-f} VsSQ_5 - F_{ex}(x) \tag{31}$$

Define the residual r_i, which has no dimensions of its own.. In accordance with the correlation between parameters and GARRs, the fault signature matrix (FSM) is obtained. FSM is shown in Table 4. For the elements M_{mn}, m is the number of rows, n is the number of columns in the matrix, and the relationship is:

$$M_{mn} = \begin{cases} 1 & Parameter \in \mathrm{ARR}_i(r_i) \\ 0 & Parameter \notin \mathrm{ARR}_i(r_i) \end{cases} \tag{32}$$

For any parameter corresponding to a lateral quantity such as $M_{1n} = [M_{11}, M_{12}, M_{13}, \cdots, M_{1n}]$, detectability D_b and isolatability I_b are:

$$D_b = \begin{cases} 1 & M_{1n} = [M_{11}, M_{12}, M_{13}, \cdots, M_{1n}] \neq [0, \cdots, 0] \\ 0 & M_{1n} = [M_{11}, M_{12}, M_{13}, \cdots, M_{1n}] = [0, \cdots, 0] \end{cases} \tag{33}$$

$$I_b = \begin{cases} 1 & M_{1n} = [M_{11}, M_{12}, M_{13}, \cdots, M_{1n}]\ is\ unique \\ 0 & M_{1n} = [M_{11}, M_{12}, M_{13}, \cdots, M_{1n}]\ is\ not\ unique \end{cases} \tag{34}$$

$$\begin{cases} r_i = \mathrm{GARR}_i = 0 & No\ fault \\ r_i = \mathrm{GARR}_i \neq 0 & Faulty \end{cases} \tag{35}$$

Preprints (www.preprints.org) | NOT PEER-REVIEWED | Posted: 18 July 2022 doi:10.20944/preprints202207.0247.v1

The FSM's non-zero elements have been identified by a distinctive hue that denotes the following:

Red: residual elements in the matrix that are not 0.

Blue: detectability element that is not 0.

Green: isolability element that is not 0.

Yellow: parameters directly related to the fault, and identified boundary line.

Oil filter clogging key parameter R_{Fil} mainly refers to residual r_1; actuator leakage key parameter R_{Ex-l} R_{In-l} mainly refers to residual r_5 r_8 respectively; landing gear selector valve reversing stuck key parameter R_{PA} mainly refers to residual r_2 r_3, R_{PB} refers to r_2 r_4, R_{AT} refers to r_3, R_{BT} refers to r_4.

Table 4. Fault signature matrix of landing gear R/E hydraulic system.

Parameter	r_1	r_2	r_3	r_4	r_5	r_6	r_7	r_8	r_9	D_b	I_b
Sp	1	0	0	0	0	0	0	0	0	1	0
R_{Fil}	1	0	0	0	0	0	0	0	0	1	0
R_{Elb}	0	1	1	1	0	0	0	0	0	1	0
R_{Che}	0	1	1	1	0	0	0	0	0	1	0
R_{Thr}	0	0	1	1	1	1	0	0	0	1	1
R_{Ex-l}	0	0	0	0	1	0	0	0	0	1	0
R_{Sli-f}	0	0	0	0	0	1	0	0	0	1	0
R_{In-l}	0	0	0	0	0	0	0	1	0	1	1
R_{Eq-f}	0	0	0	0	0	0	0	0	1	1	0
R_{PA}	0	1	1	0	0	0	0	0	0	1	1
R_{PB}	0	1	0	1	0	0	0	0	0	1	1
R_{AT}	0	0	1	0	0	0	0	0	0	1	1
R_{BT}	0	0	0	1	0	0	0	0	0	1	1
p_T	0	0	1	1	0	0	0	0	0	1	1
C_{Fil}	1	1	1	1	0	0	0	0	0	1	0
$C_{Pip-ele}$	0	1	0	0	0	0	0	0	0	1	1
C_{Lef}	0	0	0	0	0	1	0	0	0	1	0
C_{Rig}	0	0	0	0	1	0	0	0	0	1	0
C_{Rod}	0	0	0	0	1	0	0	0	0	1	0
$C_{Rodless}$	0	0	0	0	0	1	0	0	0	1	0
I_{Eq-m}	0	0	0	0	0	0	0	0	1	1	0
A_{Lef}	0	0	0	0	0	1	1	0	0	1	1
A_{Rig}	0	0	0	0	1	0	1	0	0	1	1
A_{Rod}	0	0	0	0	1	0	0	0	1	1	1
$A_{Rodless}$	0	0	0	0	0	1	0	0	1	1	1
$F_{ex}(x)$	0	0	0	0	0	0	0	0	1	1	1

4. Fault characteristic research and diagnosis

GRR and residual are the mathematical models that can most accurately describe fault variation. An examination of the A, B, C, and D types of defects follows.

Preprints (www.preprints.org) | NOT PEER-REVIEWED | Posted: 18 July 2022 doi:10.20944/preprints202207.0247.v1

Positive, negative, or 0 residuals are possible. It has no dimensions and no physical significance. According to the literature [39], the threshold is set as a symmetric type with the x-horizontal axis as the symmetric median. This is due to the fact that it is hard to predict the direction in which residuals will go before detection. Threshold deviation is defined as ε_i and the uncertainty as δ. The threshold range is:

$$\begin{cases} Upper\ threshold = r_i + \varepsilon_i \\ Lower\ threshold = r_i - \varepsilon_i \end{cases} \tag{36}$$

4.1. Fault free system sensor measurements

According to the diagnostic bond graph in Figure 11, as illustrated in Figure 12, the diagnostic simulation model is created in the LMS Imagine.Lab AMESim simulation platform. On the diagnostic bond graph, the sensor shown in the illustration is the same sensor. Measured value in the fault-free condition can be used as the standard value in the diagnostic process, and each residual value obtained after the subsequent change in the fault parameters can be compared with the corresponding threshold value to realize the diagnosis of each fault type.

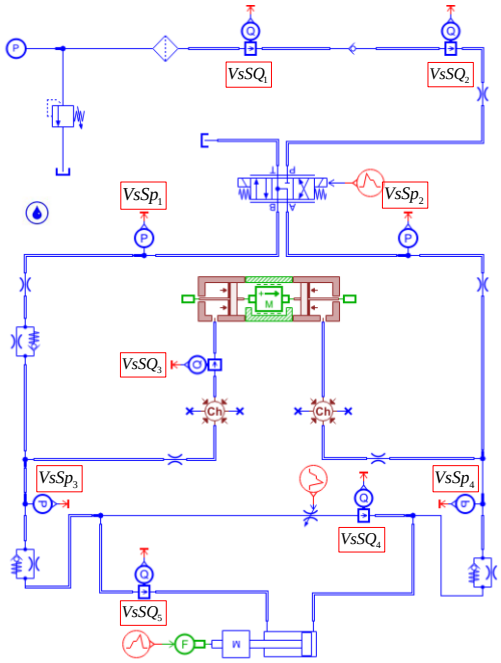

Figure 12. Diagnostic simulation model of the system.

The parameters of the resistive element can be determined by the following equation:

$$R = \frac{p_o - p_i}{Q_o - Q_i} \tag{37}$$

where p_o and Q_o are the output pressure and flow rate of the resistive element, and p_i Q_i are the input pressure and flow rate of the resistive element.

Table S5 displays some of the critical variables of the system diagnosis simulation model. Figure S1 shows sensor standard value curves from the simulation of system diagnostics, and subsequent fault diagnosis studies can be carried out by importing their curves in MATLAB/Simulink.

4.2. Filter clogged

Oil filter according to the liquidity will significantly affect liquid resistance R_{Fil}. Aviation oil filters typically come in mesh, wire gap, paper core, and sintered varieties.

Preprints (www.preprints.org) | NOT PEER-REVIEWED | Posted: 18 July 2022 doi:10.20944/preprints202207.0247.v1

Although different types of filters are frequently used in various settings, the fundamental idea behind impurity filtration remains the same: impurities are filtered through fine mesh, slits, microporous materials, etc. The filter's flow area will therefore be less when it is obstructed, increasing the liquid resistance R_{Fil}. Take the mesh structure as an example, its basic principle diagram is shown in Figure 13.

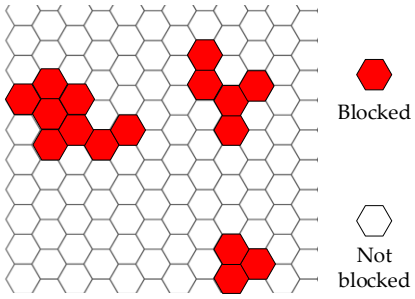

Figure 13. Basic principle of oil filter blocked.

Define the total number of pores as $P_{\max}$, where the number of blockages is P. Then the degree of blockage λ liquid resistance R_{Fil} of the oil filter is:

$$\begin{cases} \lambda = \dfrac{P}{P_{\max}} \\ R_{Fil} = \lambda R_{(Fil)\max} \end{cases} \tag{38}$$

Limit $\lambda \in [0.05, 0.95]$, when in the worst case of clogged the liquid resistance is $R_{(Fil)\max}$, according to the literature [40] to take the value of $3.2\text{x}10^{13} N \cdot s / m^5$.

When $\beta = [1, 0, 0, 0]$, the residual is obtained from GARR_1 as

$$r_1 = Sp - R_{Fil} VsSQ_1 - \frac{1}{C_{Fil}} \int_2^{15} (VsSQ_1 - VsSQ_2) dt \tag{39}$$

Threshold deviation ε_1 and threshold range corresponding to the residual r_1 is

$$\varepsilon_1 = \delta Sp + \delta R_{Fil} \left| VsSQ_1 \right| + \frac{1}{\delta C_{Fil}} \int \left| VsSQ_1 - VsSQ_2 \right| dt \tag{40}$$

$$\begin{cases} Upper\ threshold = r_1 + \varepsilon_1 \\ Lower\ threshold = r_1 - \varepsilon_1 \end{cases} \tag{41}$$

Setting the degree of blockage λ to grow linearly with time t, the liquid resistance R_{Fil} is

$$\begin{cases} \lambda = 0.05 + 0.10(t-2) \quad t \geq 2 \\ R_{Fil} = \lambda R_{(Fil)\max} \end{cases} \tag{42}$$

Figure S2 shows the computational model in MATLAB/Simulink, according to the literature [41], $Sp = 2.0685 \times 10^7\ Pa(3000\,psi)$, $C_{Fil} = 6.27 \times 10^{-15} (m^5 / N)$.

Figure 14 shows the simulation results with sampling frequencies of 1000 Hz. Set 0 to 2s as the system preparation time, from the graph, we can see that the residual r_1 exceeds the lower threshold at 5.986s, that is, the oil filter clogging fault is successfully diagnosed, and the clogging rate λ is about 0.449 at this time.

Preprints (www.preprints.org) | NOT PEER-REVIEWED | Posted: 18 July 2022 doi:10.20944/preprints202207.0247.v1

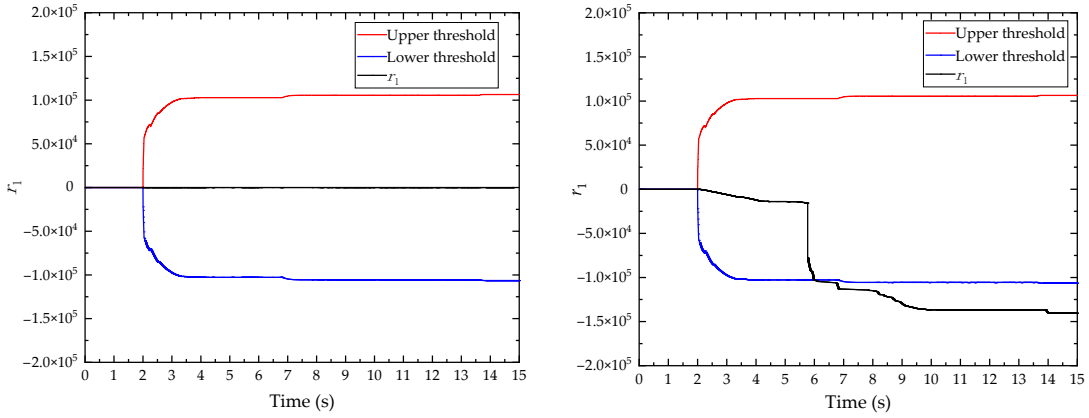

Figure 14. Simulation result of oil filter blocked: (**a**) No fault; (**b**) Fault present.

4.3. Internal and external leakage of actuator

One of the actuator's most prevalent failure types is leakage, as shown by the fundamental ideas in Figure 15. There is no escape from it; it is a mode. Generally, it is controlled by increasing tightness and performing regular inspections. Figure 15 shows the leakage flow, which is represented by the red dotted line. There are two types of leaks: internal and external. Internal leaks happen between the cylinder and piston, while external leaks happen between the piston rod and cylinder. Take the piston rod extension as an example. When high-pressure hydraulic oil forces the piston out of the actuator cylinder, flow loss will occur between these two kinds of gaps.

In the reciprocating motion of the piston of the actuator cylinder, let a point between the piston surface and the sealing gap be S, the position coordinate is x, the pressure gradient $(dp/dx) \neq 0$ and the thickness gradient $w_s = (dp/dx)_s$ at this point, therefore, the oil film thickness h_0 at point S and the hydraulic cylinder outer stroke leakage Q_0 is

$$\begin{cases} h_0 = \dfrac{\sqrt{2\mu u_0}}{9w_s} \\ Q_0 = \pi dLh_0 = \pi dL\dfrac{\sqrt{2\mu u_0}}{9w_s} \end{cases} \tag{43}$$

Where μ is the dynamic viscosity of the oil, u_0 is the velocity of the piston rod movement, d is the piston rod diameter, and L is the stroke length.

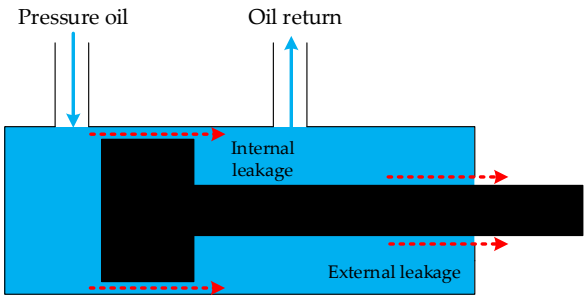

Figure 15. Basic principle of actuator leakage.

When the oil leaks inside the cylinder, set the end point of the leak as Z, the point of pressure gradient $(dp/dx) \neq 0$, thickness gradient $w_Z = (dp/dx)_Z$. When the

Preprints (www.preprints.org) | NOT PEER-REVIEWED | Posted: 18 July 2022 doi:10.20944/preprints202207.0247.v1

oil leaks outside the cylinder, set the point of atmospheric pressure gradient outside the cylinder as Y, the point of pressure gradient $(dp/dx) \neq 0$, thickness gradient $w_Y = (dp/dx)_Y$. Therefore, the oil film thickness h_1 and the return volume Q_1 are:

$$\begin{cases} h_1 = \dfrac{\sqrt{2\mu u_1}}{9w_i} \\ Q_1 = \pi dLh_1 = \pi dL\dfrac{\sqrt{2\mu u_1}}{9w_i} \end{cases} \qquad \begin{cases} Internal\ leakage:\ i = Z \\ \\ External\ leakage:\ i = Y \end{cases} \tag{44}$$

The net leakage of the piston per single cycle of reciprocating motion ΔQ is

$$\Delta Q = Q_0 - Q_1 \tag{45}$$

Set α as the leakage coefficient, and adjust the value range of α to simulate the size of the leakage:

$$\begin{cases} R_{In-l} = \alpha \Delta Q_{In-l} \\ R_{Ex-l} = \alpha \Delta Q_{Ex-l} \end{cases} \quad \alpha \geq 1 \tag{46}$$

Set the growth gradient of the leakage coefficient α a per second for internal leakage starting from 2s to 0.05. $\beta = [0,0,1,0]$, when the key parameter r_8 for diagnosing internal leakage is obtained according to GARR_8:

$$r_8 = VsSp_4 - VsSp_3 - R_{In-l}VsSQ_4 \tag{47}$$

Threshold deviation ε_8 and threshold range corresponding to the residual r_8 is

$$\varepsilon_8 = \delta|VsSp_4| + \delta|VsSp_3| + \delta R_{In-l}|VsSQ_4| \tag{48}$$

$$\begin{cases} Upper\ threshold = r_8 + \varepsilon_8 \\ Lower\ threshold = r_8 - \varepsilon_8 \end{cases} \tag{49}$$

Set the growth gradient of the leakage coefficient α a per second for internal leakage starting from 2s to 0.02. $\beta = [0,1,0,0]$, when the key parameter r_5 for diagnosing internal leakage is obtained according to GARR_5:

$$r_5 = \frac{VsSQ_3}{A_{Rig}} + \frac{VsSQ_5}{A_{Rod}} - \frac{VsSp_3 - VsSp_1}{R_{Thr}} - \frac{VsSp_3}{R_{Ex-l}} + VsSQ_4 - (C_{Rig} + C_{Rod})\frac{d(VsSp_3)}{dt} \tag{50}$$

Threshold deviation ε_5 and threshold range corresponding to the residual r_5 is

$$\varepsilon_5 = \frac{|VsSQ_3|}{\delta A_{Rig}} + \frac{|VsSQ_5|}{\delta A_{Rod}} + \frac{|VsSp_3 - VsSp_1|}{\delta R_{Thr}} + \frac{|VsSp_3|}{\delta R_{Ex-l}} + \delta|VsSQ_4| + \delta(C_{Rig} + C_{Rod})\left|\frac{d(VsSp_3)}{dt}\right| \tag{51}$$

$$\begin{cases} Upper\ threshold = r_5 + \varepsilon_5 \\ Lower\ threshold = r_5 - \varepsilon_5 \end{cases} \tag{52}$$

Figures S3 S4 depict the actuator cylinder internal and exterior leakage calculation models. Figure 16 shows simulation results. The figure shows that the residual r_8 exceeds the lower threshold at 10.566s, diagnosing an internal leakage fault with the coefficient α of 1.428; the residual r_5 exceeds the lower threshold at 8.069s, diagnosing an external leakage fault with the coefficient α of 1.121.

Preprints (www.preprints.org) | NOT PEER-REVIEWED | Posted: 18 July 2022 doi:10.20944/preprints202207.0247.v1

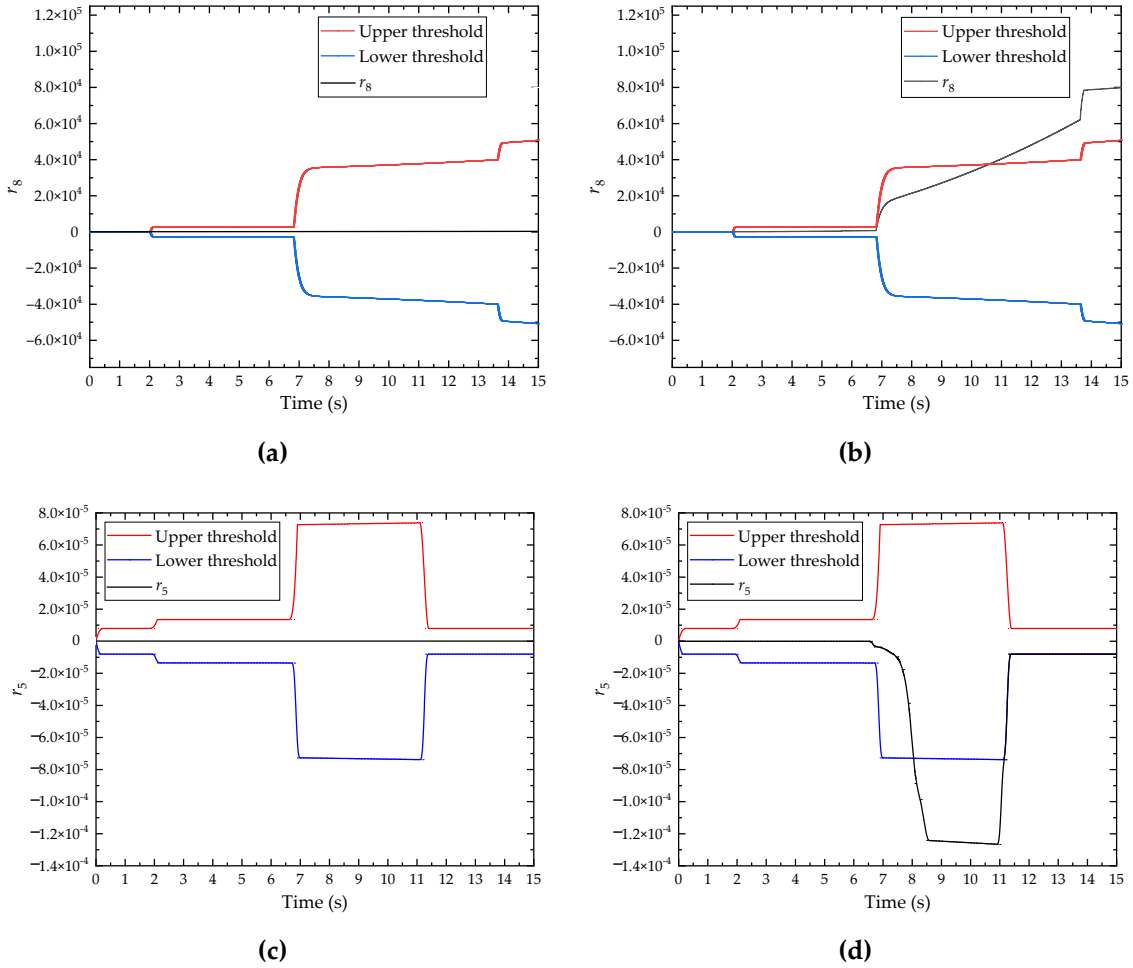

Figure 16. Simulation result of internal leakage of actuator: (**a**) No fault; (**b**) Fault present;

Simulation result of external leakage of actuator: (**c**) No fault; (**d**) Fault present.

4.4. Landing gear selector valve reversing stuck

Landing gear selector valve has 3 operational states [42]: Neutral, Left, and Right. Using the Left as an example, we can see from the analysis above that at this moment, we do not take the liquid resistance R_{PA} and R_{BT} into consideration, they are constant fixed values, the fault diagnosis object is the liquid resistance R_{PB} and R_{AT}. R_{PB} corresponds to r_2 and r_4, R_{AT} corresponds to r_3. Shifting to the right reverses the object of research and control invariant liquid resistance. Nonlinear liquid resistance as liquid flows through the slide-valve orifice can be used to compute individual liquid resistances:

$$R = \frac{1}{C_d W_x \sqrt{\frac{2}{\rho}} \Delta p^{-\frac{1}{2}}} \tag{53}$$

C_d is the flow coefficient of the slide valve orifice, generally taken as 0.7; W is the circumferential length of the valve orifice, x is the opening of the valve orifice, W_x maximum 0.3mm; ρ is the fluid density, taken as $850\,kg/m^3$; Δp is the differential pressure, measured to take the value. By changing the valve opening x for fault simulation and injection, let the change of x satisfy:

$$x = 0.98 - 0.05(t-2) \qquad t \geq 2 \tag{54}$$

Preprints (www.preprints.org) | NOT PEER-REVIEWED | Posted: 18 July 2022 doi:10.20944/preprints202207.0247.v1

$\beta=[0,0,0,1]$, the set of residuals r_2, r_3, r_4 is obtained according to GARR_2, GARR_3, GARR_4:

$$\begin{cases} r_2 = \dfrac{1}{C_{Fil}}\int(VsSQ_1 - VsSQ_2)dt - \dfrac{1}{nC_{Pip-ele}}\int(VsSQ_2 - \dfrac{VsSp_1}{R_{PA}} - \dfrac{VsSp_2}{R_{PB}})dt - (R_{Elb}+R_{Che})VsSQ_2 \\ r_3 = \dfrac{\dfrac{1}{C_{Fil}}\int(VsSQ_1 - VsSQ_2)dt - (R_{Elb}+R_{Che})VsSQ_2 - VsSp_1}{R_{PA}} + \dfrac{VsSp_3 - VsSp_1}{R_{Thr}} - \dfrac{VsSp_1 - p_T}{R_{AT}} \\ r_4 = \dfrac{\dfrac{1}{C_{Fil}}\int(VsSQ_1 - VsSQ_2)dt - (R_{Elb}+R_{Che})VsSQ_2 - VsSp_2}{R_{PB}} - \dfrac{VsSp_2 - VsSp_4}{R_{Thr}} - \dfrac{VsSp_2 - p_T}{R_{BT}} \end{cases} \tag{55}$$

Threshold deviation ε_2 ε_3 ε_4 and threshold range corresponding to the residual r_2, r_3, r_4 is

$$\begin{cases} \varepsilon_2 = \dfrac{1}{\delta C_{Fil}}\int|VsSQ_1 - VsSQ_2|dt + \dfrac{1}{n\delta C_{Pip-ele}}\int\left|VsSQ_2 - \dfrac{VsSp_1}{R_{PA}} - \dfrac{VsSp_2}{R_{PB}}\right|dt + \delta(R_{Elb}+R_{Che})|VsSQ_2| \\ \varepsilon_3 = \dfrac{\dfrac{1}{\delta C_{Fil}}\int|VsSQ_1 - VsSQ_2|dt + \delta(R_{Elb}+R_{Che})|VsSQ_2| + \delta|VsSp_1|}{R_{PA}} + \dfrac{|VsSp_3 - VsSp_1|}{\delta R_{Thr}} + \dfrac{|VsSp_1 - p_T|}{\delta R_{AT}} \\ \varepsilon_4 = \dfrac{\dfrac{1}{\delta C_{Fil}}\int|VsSQ_1 - VsSQ_2|dt + \delta(R_{Elb}+R_{Che})|VsSQ_2| + \delta|VsSp_2|}{R_{PB}} + \dfrac{|VsSp_2 - VsSp_4|}{\delta R_{Thr}} + \dfrac{|VsSp_2 - p_T|}{\delta R_{BT}} \end{cases} \tag{56}$$

$$\begin{cases} Upper\ threshold = r_2 + \varepsilon_2 \\ Lower\ threshold = r_2 - \varepsilon_2 \end{cases} \quad \begin{cases} Upper\ threshold = r_3 + \varepsilon_3 \\ Lower\ threshold = r_3 - \varepsilon_3 \end{cases} \quad \begin{cases} Upper\ threshold = r_4 + \varepsilon_4 \\ Lower\ threshold = r_4 - \varepsilon_4 \end{cases} \tag{57}$$

Figs. S5, S6, and S7 depict the calculation model for a landing gear selector valve spool jam. Figures 17, 18 and 19 illustrate the simulation results. As can be seen from the graphs, r_2 exceeded the lower threshold limit at 4.8034s, r_3 exceeded the lower threshold limit at 5.486s, and r_4 exceeded the upper threshold limit at 2.369s, all of which detected the spool sticking fault.

However, the sensitivity of detection differs for different residuals, with r_4 being the most sensitive. r_2 has an openness x of 0.73983 for R_{PB} detection, r_4 has an openness x of 0.96155 for it. r_3 has an openness x of 0.8057 for R_{AT} detection.

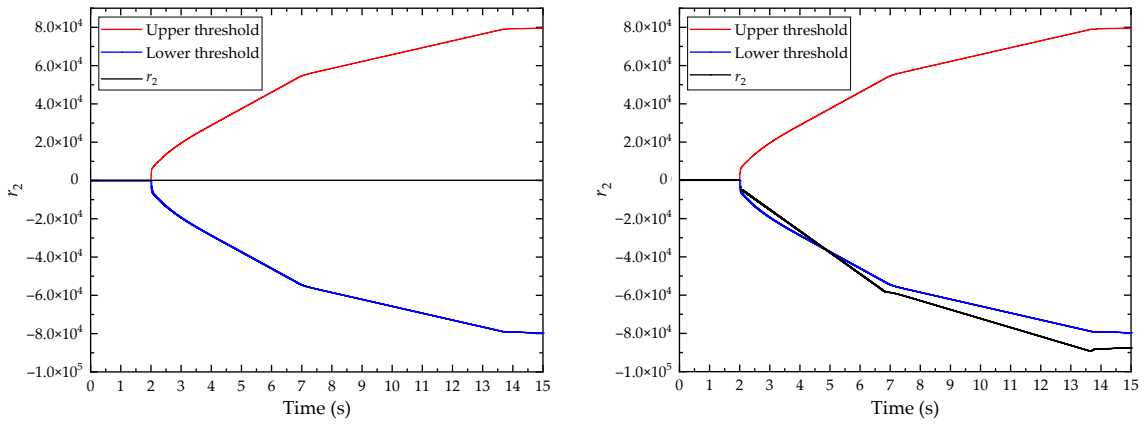

Figure 17. Simulation result of valve reversing stuck' residuals r_2 : (**a**) No fault; (**b**) Fault present.

Preprints (www.preprints.org) | NOT PEER-REVIEWED | Posted: 18 July 2022 doi:10.20944/preprints202207.0247.v1

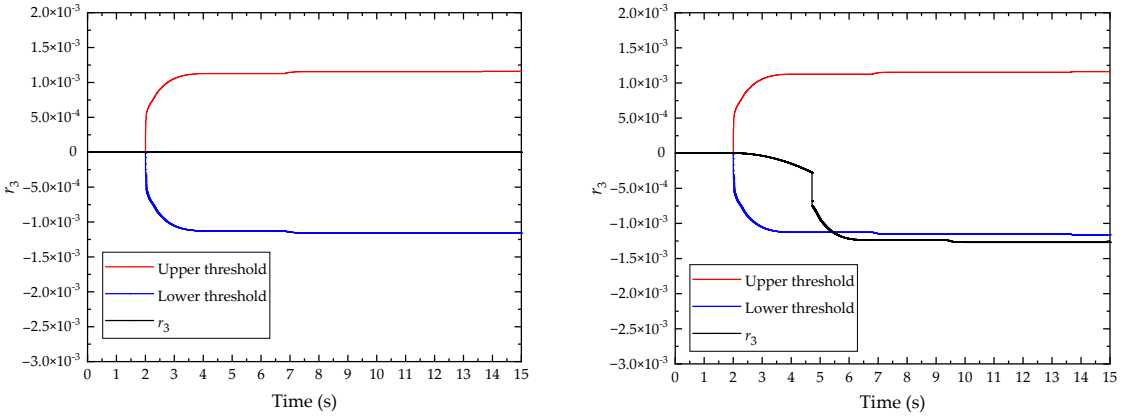

Figure 18. Simulation result of valve reversing stuck' residuals r_3 : (**a**) No fault; (**b**) Fault present.

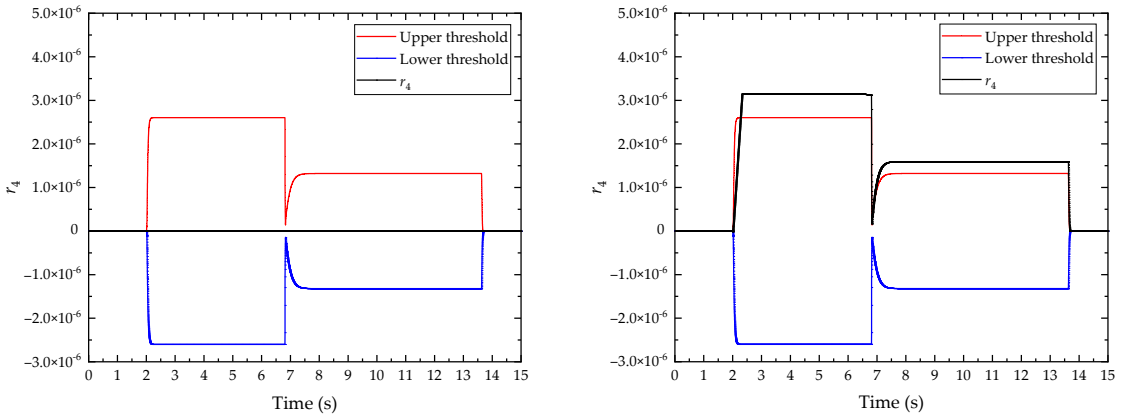

Figure 19. Simulation result of valve reversing stuck' residuals r_4 : (**a**) No fault; (**b**) Fault present.

5. Conclusions

(1) Based on the power bond graph modeling technique, the landing gear R/E hydraulic system was developed. Ignore the auxiliary factors after modeling at the component level, then streamline the overall modeling at the system level. Thus, GARRs and fault analysis can be produced more easily.

(2) The system diagnostic bond graph yields the GARRs. By adjusting parameter functions, the model can simulate asymptotic hydraulic resistance fault injection.

(3) FSM are derived from the GARRs. Using the FSM, the GARR level localization of the above injected faults can be achieved and further detected, and all parameters are detected and isolated.

(4) To detect faults, the corresponding residual is obtained from the localized GARR and is compared with the matching threshold. Since the change direction of the residuals cannot be predicted in advance, the symmetric threshold generation method proposed by Sawan Kumar with the x-axis as the symmetric median and the uncertainty δ are applied to generate the corresponding diagnostic thresholds for fault detection of type A, B, C, and D faults considered by the Boolean logic variable β . MATLAB/Simulink is used to construct computational models that detect faults for every type of fault studied.

(5) Landing gear selector valve reversing stuck for example, for the same type of fault if you can generate different residuals, the sensitivity of different residuals detection will

 doi:10.20944/preprints202207.0247.v1

be somewhat different, it is worth to carry out further research, perhaps to provide new ideas for fault diagnosis and stateful inspection.

Supplementary Materials: The following supporting information can be downloaded at: Table S1: Parameter meanings of hydraulic source components; Table S2: Parameter meanings of actuator and transfer cylinder; Table S3: Parameter meanings of other components; Table S4: Parameter meanings of hydraulic pipe; Table S5: Some key parameters of fault simulation diagnosis model; Figure S1: Sensor standard value curves; Figure S2: Calculation model of r_1 and its threshold; Figure S3: Calculation model of r_8 and its threshold; Figure S4: Calculation model of r_5 and its threshold; Figure S5: Calculation model of r_2 and its threshold; Figure S6: Calculation model of r_3 and its threshold; Figure S7: Calculation model of r_4 and its threshold.

Author Contributions: Manuscript Writing, Y.C. and S.D.; manuscript Revision, Y.L.; simulation test: S.D. and X.L.; project Funding: Y.C.; reference and data collation: Z.Z. and X.W. All authors have read and agreed to the published version of the manuscript.

Funding: This research was funded by [the Aero-Science Fund of China] grant number [20200033052001] and [Nanjing University of Aeronautics and Astronautics Postgraduate Innovation Base Open Fund] grant number [kfjj20200725].

Institutional Review Board Statement: Not applicable.

Informed Consent Statement: Not applicable.

Data Availability Statement: Not applicable.

Conflicts of Interest: The authors declare no conflict of interest.

References

1. He, X; Ai, J; Song, Z. Shimmy Simulation and Virtual Verification for Civil Aircraft Landing Gear Airworthiness Certification. *Journal of Mechanical Engineering*. **2018**, 54, 179-184.
2. Yin, Y; Nie, H; Wei, X; Ni, H. Dynamic analysis and test of aircraft landing gear retraction and extension system. *Journal of Vibration, Measurement & Diagnosis.* **2016**, 36, 641-646.
3. Guo, A; Zhou, Z; Zhu X; Bai, F. Research on aircraft takeoff and landing performance calculation method based on flight simulation. *Journal of Northwestern Polytechnical University.* **2019**, 37, 433-442.
4. Wei, J; Chen, Z. *Aircraft systems;* Tsinghua University Press: Beijing, China, **2016**; 409-416.
5. Li, Y. *Aircraft hydraulic transmission and control*; Science Press: Beijing, China, **2009**; 161–169.
6. *Boeing, Statistical Summary of Commercial Jet Airplane Accidents Worldwide Operations 1959–2017*; 2017.
7. *Airbus, A Statistical Analysis of Commercial Aviation Accidents 1958-2018*; 2018.
8. *EASA, Annual Safety Review 2020*; 2020.
9. *ICAO, State of Global Aviation Safety;* 2019.
10. Han, X. Research on Lightweight Distributed Neural Network Technology for Fault Diagnosis. Master's Thesis, Zhejiang University, Hangzhou, China, **2022**.
11. Yin, H. Research on Model-Based Fault Diagnosis Method for Open-Switch Faults of Switch Tube of Three-Phase Voltage Source Inverters. Master's Thesis, University of Electronic Science and Technology, Chengdu, China, **2021**.
12. Zhao, J; Xing, L; Ma, X; Wang, Y; Gao, D; Du, G. Impact-Rubbings Dynamics Behavior of Magnetic-Liquid Double Suspension Bearing in Electromagnetic Failure Model. *Appl. Sci.* **2021**, 11, 6345.
13. Ezhilarasu, C; Jennions, I. A System-Level Failure Propagation Detectability Using ANFIS for an Aircraft Electrical Power System. *Appl. Sci.* **2020**, 10, 2854.
14. Shen, K; Zhao, D. Fault Diagnosis for Aircraft Hydraulic Systems via One-Dimensional Multichannel Convolution Neural Network. *Actuators*. **2022**, 11, 182.
15. Zhang, L; Feng, F; Liu, X; Wang, M. Research on Fault Detection and isolation method for Typical Hydraulic System. *Journal of System Simulation*. **2018**, 30, 1818-1825.
16. Yu, M; Lu, H; Wang, H; Xiao, C; Lan, D. Compound Fault Diagnosis and Sequential Prognosis for Electric Scooter with Uncertainties. *Actuators*. **2020**, 9, 128.
17. Wang, J; Wang, Z; Ma, X; Zhang, C. Multi-fault coupling analysis and decoupling approach for diesel engine lubrication system. *Journal of Harbin Engineering University*. **2021**, 42, 825-832.
18. Wang, J; Qian, Z; Chen, M; Zhou, L; Wang, L. Research on Fault Diagnosis of Bond Graph Model Based on Temporal Causal Graph. *Control Engineering of China*. **2017**, 24, 2443-2449.
19. Wang, J; Qian, Z; Chen, M; Wang, L. Fault diagnosis of driven train system of wind turbine based on analytical redundancy relations. *Power System Protection and Control.* **2017**, 45, 41-47.

20. Zhang, X; Wen, H; Chen, J; Zhang, H; Ji, C. Dynamic characteristics of the spraying pressure for a precise intermitient spraying system using bond graph theory. *Journal of China Agricultural University*. **2021**, 26, 162-172.
21. Medjaher, K; Samantaray, A; Bouamama, O. Diagnostic Bond Graphs for Direct Residual Evaluation. International Conference on Bond Graph Modeling and Simulation (ICBGM'05), New Orleans, Louisiana, U.S.A, 23-26 Jan.2005.
22. Wei, C; Geng, H. Application of analytical redundancy relation method in fault diagnosis and isolation of diesel fuel system. *Journal of Naval University Of Engineering*. **2021**, 33, 67-74.
23. Djeziri, M; Bouamama, B; Merzouki, R. Modelling and robust FDI of steam generator using uncertain bond graph model. *Journal of Process Control*. **2009**, 19, 149-162.
24. Du, M; Cai, J; Liu, L; Chen, P. ARRs based sensor placement optimization for fault diagnosis. *Procedia Engineering*. **2011**, 16, 42-47.
25. Liu, W; Li, W; Zhang, X; Liu, C. Fault diagnosability evaluation of deep space exploration spacecraft based on graph theory. *Control Theory & Applications*. **2019**, 36, 2074-2084.
26. Liu, W; Liu, C. On Fault Diagnosis of Satellite Attitude Control System Based On ARRs. Proceedings of the 33rd Chinese Control Conference, Nanjing, Jiangsu, China, 28-30 Jul.2014.
27. Sanchez, H; Escobet, T; Puig, V; Odgaard, P. Fault Diagnosis of an Advanced Wind Turbine Benchmark Using Interval-Based ARRs and Observers. *IEEE Transactions on Industrial Electronics.* **2015,** 62, 3783-3793.
28. Sanchez, H; Escobet, T; Puig, V. Fault Diagnosis of Advanced Wind Turbine Benchmark using Interval-based ARRs and Observers. Proceedings of the 19th World Congress The International Federation of Automatic Control, Cape Town, South Africa, 24-29 Aug.2014.
29. Sia, K; Namaane, A; M'Sirdi, N. A new structural approach for ARRs generation from linear & linearized bond graphs. 2011 International Conference on Communications, Computing and Control Applications (CCCA), 3-5 Mar.2011
30. Low, C; Wang, D; Arogeti, S; Luo, M. Quantitative Hybrid Bond Graph-Based Fault Detection and Isolation. *IEEE Transactions on Automation Science and Engineering*. **2010**, 7, 558-569.
31. Meng, k; Jie, S; Qing, T; Ding, H. Aircraft hydraulic power system design for low temperature. CSAA/IET International Conference on Aircraft Utility Systems (AUS 2020), Tianjin, China, 18-21 Sep.2020.
32. Yin, Y. Dynamics and Reliability Analysis of Retraction of Landing Gear. Doctor's Thesis, Nanjing University of Aeronautics and Astronautics, Nanjing, China, **2017**.
33. *Air Transport Association of America. ATA 100 specification for manufacturers'technical data.* U.S.A, 1999.
34. Liu, B. Bond Graph Modeling and Simulation of Wind-Tide Hybrid Drive System. Master's Thesis, Xi'an University of Technology, Xi'an, China, **2018**.
35. Qian, Z. Modeling and Fault Diagnosis of Wind Turbine System based on Bond Graph. Master's Thesis, Hunan University of Science and Technology, Xiangtan, China, **2016**.
36. Lv, X. Cost Efficient Sensor Positions Determination For Human Activity Recognition. Master's Thesis, Huazhong University of Science & Technology, Wuhan, China, **2019**.
37. Mo, H; Li, Y. Fault Diagnosis Based on Interval Analytic Redundancy Relation. *Journal of Nanjing University of Aeronautics & Astronautics.* **2021**, 53, 972-980.
38. Wang, Z. *Bond graph theory and its application in system dynamics*; Harbin Engineering University Press: Harbin, China, **2000**; 38–46.
39. Dutta, S; Kumar, S; Saha, T; Ghoshal, S. Determination of the Degradation Pattern of Pump Using Two-Phase Diagnostic Bond Graph. Lecture Notes in Mechanical Engineering of Springer, Recent Advances in Mechanical Engineering Select Proceedings of NCAME 2019.
40. Ma, J. Reliability Research of Certain Aircraft Hydraulic System Based on GO Methodology. Master's Thesis, Dalian University of Technology, Dalian, China, **2020**.
41. *Air Transport Association of America. ATA iSpec 2200 information standards for aviation maintenance.* U.S.A, 2005.
42. Yin, Y; Nie, H; Wei, X; Ni, H. Performance analysis of landing gear retraction and extension system under the influence of multiple factors. *Journal of Beijing University of Aeronautics and Astronautics*. **2015**, 41, 953-960.